Author's version 2018 02 09
Published in Joule

Influence of charge transport layers on open-circuit voltage and hysteresis in perovskite solar cells

Sandheep Ravishankar,[1ε] Saba Gharibzadeh,[2,3ε] Cristina Roldán-Carmona,*[2] Giulia Grancini,[2] Yonghui Lee[2], Maryline Ralaiarisoa[4,5], Abdullah M. Asiri,[6] Nobert Koch[4,5], Juan Bisquert*[1,7] and Mohammad Khaja Nazeeruddin*[2]

[1] Institute of Advanced Materials (INAM), Universitat Jaume I, 12006 Castelló, Spain
[2] GMF, Institute of Chemical Sciences and Engineering, EPFL Valais, Rue de L'Indutrie, 1951 Sion, Switzerland.
[3] Department of Physics, Tarbiat Modares University, P.O. Box 14115-175, Tehran-Iran
[4] Humboldt-Universität zu Berlin, Institut für Physik & IRIS Adlershof, Berlin, Germany
[5] Helmholtz-Zentrum Berlin für Materialien und Energie, Devision Renewable Energies, Berlin, Germany
[6] Center of Excellence for Advanced Materials Research (CEAMR), King Abdulaziz University, P. O. Box 80203, Jeddah 21589, Saudi Arabia
[7]Department of Chemistry, Faculty of Science, King Abdulaziz University, Jeddah, Saudi Arabia

[ε]Equal contributing first authors.

*Corresponding authors E-mail: mdkhaja.nazeeruddin@epfl.ch, bisquert@uji.es, cristina.roldancarmona@epfl.ch

SUMMARY

Perovskite materials have experienced an impressive improvement in photovoltaic performance due to their unique combination of optoelectronic properties. Their remarkable progression, facilitated by the use of different device architectures, compositional engineering and processing methodologies, contrast with the lack of understanding of the materials properties and interface phenomena. Here we directly target the interplay between the charge transporting layers (CTL) and

open-circuit potential (V_{oc}) in the operation mechanism of the state-of-the-art $CH_3NH_3PbI_3$ solar cells. Our results suggest that the V_{oc} is controlled by the splitting of quasi-Fermi levels and recombination inside the perovskite, rather than being governed by any internal electric field established by the difference in the CTL's work functions. In addition, we provide novel insights into the hysteretic origin in PSCs, identifying the nature of the contacts as a critical factor in defining the charge-accumulation at its interface, leading to either ionic, electronic or mixed ionic-electronic accumulation.

INTRODUCTION

Despite the impressive improvement in device performance[1-8], the operating mechanism that governs the high V_{oc} and short circuit current (J_{sc}) in perovskite photovoltaics remains unclear. Perovskite solar cells (PSCs) suffer from variations in the current-voltage behaviour based on specific experimental parameters, including pre-biasing, light intensity, scan direction and rate, the set of which have been referred to as dynamic hysteresis[9]. Early studies considered such dynamic hysteresis[10] as the result of a charge collection limitation, conceiving device models in which the transport of charge-carriers arises from the built-in electric field, generated through the perovskite layer and modified by the mobile ions[11,12]. Nevertheless, the recent progression in materials processing[13-19] suggests a different scenario, as the state-of-the-art devices possess excellent transport and collection properties, with little to no variation in the photocurrent throughout the scan. In addition, a recent correlation between TiO_2/perovskite interface and the output voltage in perovskite solar cells (PSCs)[20](Rong, Yaoguang, et al. "Tunable hysteresis effect for perovskite solar cells." *Energy & Environmental Science* 10.11 (2017): 2383-2391.– DOI: 10.1039/C7EE02048A) opens the question of the

role of interfaces in the device operation, calling for deeper investigations in their operation mechanism, with special emphasis on how variations in recombination and/or accumulation at the interfaces affect the hysteretic trends. In this article, we answer some of these questions by investigating the role of the contacts in the transport and recombination of state-of-the-art PSCs. Devices with identical architecture but modified electron transporting layer (ETL) interface have been examined, using as device configuration FTO/ *ETL* / $CH_3NH_3PbI_3$ / Spiro-OMeTAD /Au architecture, where different contacts have been carefully chosen: i) *FTO/compact-*TiO_2*/meso-*TiO_2; ii) *FTO/compact-*TiO_2 and iii) *FTO* electrode (ETL-free cell).

RESULTS

Figure 1A presents a schematic diagram of the cell architecture along with the cross-sectional scanning electron microscopy (SEM) images in Figure 1B obtained for each layout. In all cases, the perovskite thickness is ~300 nm, including the mesoporous based configuration. Interestingly, similar micro-structure and layer morphology could be observed for all architectures, independently from the electron selective contact, as revealed in Figure 1C. In addition, the optical properties of the perovskite films and the X-ray diffraction (XRD) patterns (Figure 1D) were also preserved, showing identical absorption spectra and diffraction patterns corresponding to $CH_3NH_3PbI_3$ tetragonal phase[21] (see also Figure S1). Overall, these results confirm the formation of perovskite films with comparable crystalline quality and optical properties, which is of extreme importance in the upcoming comparative analysis.

The current-voltage (*J−V*) curves and the external quantum efficiency (*EQE)* of the as prepared solar cells were also analysed. Figures 2A and 2B show the typical performance of three representative cells corresponding to each device configuration

(the characteristic solar cells parameters are reported in Table 1). In agreement with previous works, cells employing a mesoscopic architecture exhibit the best photovoltaic performance (PCE = 18.75%), followed by the planar cells (PCE = 16.25%) and the ETL-free devices (PCE = 14.03%). Interestingly, J_{sc} hardly changed with the cell configuration, leading to values over 21 mA·cm^2 in all cases. These results agree with the EQE spectra exhibited in Figure 2B, which demonstrates a high photon-to-current conversion over 80 % for the entire visible spectra, even for the ETL-free device. Nevertheless, the most remarkable value is obtained for the V_{oc}, remaining close to $1V$ in all cases. Such a large V_{oc} obtained for the ETL-free cells is in contradiction to previous seminal works[15] where a large reduction upon removal of the TiO_2 layer (~0.75 V) was observed and attributed to a reduced built-in potential, generally associated to the non-selectivity of the contact. More recently, a similar behaviour was also observed by Juarez-Perez *et al.* but charge collection was severely reduced, in contrast to our result[22]. Figure 2C, 2D and Table 1 summarize the photovoltaic performance obtained from more than 40 devices. As deduced from the data, the contact layer is mostly affecting the FF of the cell, which decreases considerably when using a less-selective FTO contact, while *Jsc* and *Voc* remain very similar. Comparable results have been also observed for cells containing the mixed cation/mixed halide $(FAPbI_3)_{0.85}(MAPbBr_3)_{0.15}$ perovskite (FA = formamidinium), as is illustrated in Figure S2 (see also Table S1). Noteworthy, although slight differences in *Jsc* and *Voc* can be observed for this perovskite composition, a remarkable high *Voc* average value over 0.8 V (with a maximum of 0.96 V) is obtained for the ETL-free cell, further generalizing our previous observations.

To verify the electronic structure of the different contact layers, we analyzed them by ultraviolet photoelectron spectroscopy (UPS). The results are presented in Figure S3

and the extracted work functions are also illustrated in Figure 2D, in comparison with the Voc. As expected, the FTO layer has the highest work function (-5.22 eV), followed by the blocking TiO_2 (-4.36 eV) and the mesoporous TiO_2 layer (-4.33 eV). Surprisingly, no apparent relation between the obtained *Voc* and the work function of the contact can be deduced. This is also observed when inserting a different ETL material such as compact-SnO_2 layer (WF=-4.93 eV), which also gives unexpected high *Voc* values close to 1V (see Figure S4).

To get insight into the electronic operation of the contacts, we investigated the hysteresis features and capacitive nature of these devices via impedance spectroscopy (IS). Figure 3A shows the *J-V* curves obtained for the three systems measured under scan rates ranging from 10 to 200 mV/s. In all cases, the hysteresis loop between forward-reverse (FR) scans 'opens up' and scales with the scan rate, as typically occurs in a capacitive discharge superimposed onto the steady-state curve. We note that this effect is maximized in the planar c-TiO_2 cells but minimized for the mesoscopic architecture, suggesting meso-TiO_2 as the main factor responsible for reducing the overall hysteresis, like often reported in literature[23]. However, upon removal of the c-TiO_2 layer, the hysteresis is again reduced except for very fast scans, denoting c-TiO_2/perovskite as the real dominant interface (see Figure S5)[24]. Surprisingly, the FTO/perovskite interface also showed strong capacitive trends, indicating a similar mechanism.

DISCUSSION

According to established photovoltaic knowledge, when a semiconductor light absorber sandwiched between two contacts of very different work function comes to equilibrium, the difference of work functions implies a built in electrical field that has a major role in

the transport and extraction of charge. This is usually termed the p-i-n model. On the other hand, 25 years of study of dye-sensitized solar cells and similar devices clearly showed that many solar cells absorb the difference of work functions at the absorber/contact interface, and the electrical field in the device plays a minor role. [Ref. Juan Bisquert, The Physics of Solar Cells: Perovskites, Organics, and Photovoltaic Fundamentals", CRC Press 2017]. Here we show that this is a main principle of operation of the perovskite solar cell, since the V_{oc} remains stable over a striking modification of work function of the electron selective contact, that has the same variation as the V_{oc} itself, as shown in Fig. 2d. Independently of the built-in electric field across the perovskite, mesoporous morphology, and the difference of work functions across the interfaces, each selective contact will follow the Fermi level of the respective carrier, implying that the main control of open-circuit voltage is established by recombination. [U. Würfel, A. Cuevas and P. Würfel, "Charge Carrier Separation in Solar Cells," in IEEE Journal of Photovoltaics, vol. 5, no. 1, pp. 461-469, Jan. 2015. doi: 10.1109/JPHOTOV.2014.2363550]. This view of the device is furthermore consistent with the results of Kelvin probe force microscopy (KPFM) on cross sections of planar methylammonium lead iodide that show a flat potential distribution in the absorber layer while most of the potential drops are located at selective contact interfaces. ["Local Time-Dependent Charging in a Perovskite Solar Cell" Victor W. Bergmann, Yunlong Guo, Hideyuki Tanaka, Ilka M. Hermes, Dan Li, Alexander Klasen, Simon A. Bretschneider, Eiichi Nakamura, Rüdiger Berger, and Stefan A. L. Weber, ACS Applied Materials & Interfaces 2016 8 (30), 19402-19409].

Under cycling conditions of 10 mV/s, our systems show high V_{oc} values for both FR and RF scans. This opposes the general assumption that a built-in electric field generated by the difference in the work functions of the two contacts mediates the charge collection.

On the contrary, it demonstrates that the built-in electric field is not a major factor governing the extraction of carriers, while carrier transport to contacts is mainly due to diffusion, probably granted by the extremely large diffusion length in these materials. As large charge accumulation combining ionic and electronic charge occurs at the outer interfaces, for state-of-the-art devices, hysteretic variations can be directly correlated to the nature of the perovskite crystal in contact with the selective layers, which further underlines the importance of understanding the capacitive trends in these devices.

Figure 3B presents the evolution of the capacitance obtained for each device configuration as a function of frequency (in the dark), at different applied voltages. In general, the capacitance shows a stable plateau at high frequency due to dielectric relaxation in the bulk, and low frequency large values that grow further with the applied voltage, directly probing the contact properties. Importantly, the low frequency value increases over 2 orders of magnitude from 10 µF at low frequencies (~100 mHz) to a maximum capacitance of 10 mF for ~ 1 V. We interpret this capacitance as an accumulation layer of ionic (cations) and electronic carriers (holes) at the c-TiO_2 contact with the perovskite[25]. The capacitance for ion-accumulation is described by the Guoy-Chapman model, whose voltage-dependence for voltages above k_BT/q is given by

$$C = \left(\frac{z^2 q^2 n_i^0 \varepsilon_r \varepsilon_0}{2k_B T}\right)^{1/2} \cdot \exp\left(\frac{zqV}{m_C k_B T}\right) \qquad (1)$$

with z being the charge number of the ions, q the electronic charge, n_i^0 the ionic concentration in the bulk, and ε_r and ε_0 the relative and vacuum dielectric constants respectively. m_C is a capacitive exponent with the value 2. However, a similar equation is also used for the accumulation of majority carriers at the interface[26], again with $m_C = 2$, hindering the distinction between ionic and electronic accumulation through

only capacitance measurements. In our case, there is a difference in the way the low frequency capacitance changes with voltage between the different electron-contacts samples. The cells containing meso-TiO_2 exhibit a sharp increase after 0.6 V. Planar c-TiO_2 cells show a similar evolution, although a negative capacitance region is perceived, whose onset is characterised by the downward spike, located around 100 Hz. The negative capacitance, well documented in literature, is interpreted as the accumulation and subsequent discharge of both ionic and electronic carriers (holes) at the TiO_2/perovskite interface[27]. Finally, ETL-free samples do not show the negative capacitance trend, but a continuous and exponential evolution of the low frequency capacitance with voltage, noted in Figure 3C. We can therefore conclude that low frequency capacitance at low and very high voltage show similar trends in the three different PSCs, but the intermediate voltages and the larger frequency region variations, indicate dynamic modifications in charge accumulation (ionic/electronic) that have significant consequences on the nature and timescales in a transient experiment, altering the hysteretic trends considerably. This observation correlates well with the different dynamic hysteresis responses observed previously.

To investigate the processes at the perovskite/ETL interface, we performed a dynamical optical investigation by means of transient absorption spectroscopy (TAS) in the nanosecond domain, as depicted in Figure 4. We monitored the TAS spectral evolution of the three different samples upon excitation with a light pulse at 600nm, ensuring a light penetration depth of less than 200 nm[28]. Note that we keep the excitation density constant on the three samples, which have the same thickness, ensuring that a similar carrier density is generated. As reported in the Figure 4A-C, a negative band peaking at 760 nm appears, which is assigned to the photobleaching (PB), due to state filling of the conduction and valence band. Notably, the PB signal is proportional to the density of

charges and its dynamical evolution reflect the charge dynamics. The PB band decreases in the time range investigated, as shown by the normalized dynamic at 760nm probe wavelength presented in Figure 4D. It reveals a fast decay with a time constant of t=100 ns, accompanied by a longer component which does not decay in our temporal window (1.5 µs) (a comparison of the decay in the 100ns range is reported in the inset of Figure 4B). Since we use an excitation density of around 50nJ/cm^2 corresponding to a charge density of around 10^{17}cm^{-3}, most of the traps are expected to be filled, thus the PB decay mainly mirrors the electron hole recombination. However, the PB signal persists on a longer timescale. As already observed by Leijtens T. *et al*, the long living component appearing in the TAS as well as in transient photocurrent measurements, can be related to trap-mediated recombination, i.e. trapped electrons or holes[29]. Considering the same optical density for the three films and the same excitation density used, we can infer from the initial spectra (at 0-200 ns time window) that the photoinduced charge density at the compact-TiO_2/perovskite interface is slightly higher. However, for all cases, the long living component, sometimes also visible in photoluminescence measurements and still debated, can be related to the presence of long-living accumulated charges (possibly holes)[30], located at the perovskite /ETL surface. Interestingly, the signal evolution (i.e. time constant) and magnitude of the long living component is similar in all cases, providing a clear indication that the interface charge dynamics in the ns-us time scale, relevant for the photovoltaic action in terms of charge collection, do not considerably differ comparing meso-TiO_2, c-TiO_2 or FTO interfaces. On the other side, on the shorter time scale, the PB of the meso-TiO_2 interface decays slower (a time constant of 50 ns is retrieved from fitting, as shown in Table 2), that might reflect a reduce electron hole recombination possibly due to reduced charge accumulation at this interface. This observation is in agreement with the slightly higher

V_{oc} that this sample presents over the others. A direct link with the device behaviour is rather challenging, however, the reduced charge accumulation at the meso-TiO_2 interface might be a possible reason, among others, of the minimized dynamic hysteresis response for the mesoporous-based solar cell. Further work is ongoing to elucidate the interface dynamics and better establish a connection to the device scale. We can therefore conclude that, while it is widely believed that the role of selective contacts towards photovoltage operates by controlling the built-in voltage, here we demonstrate that it rather depends on the internal recombination and splitting of Fermi levels inside the perovskite material. Our results indicate that the electric field is not the dominant charge extraction mechanism for the photocarriers, and very different electron contacts based on metal oxide/perovskite interface can behave similarly. Furthermore, the nature of the contact can drastically influence the dynamic response of charge accumulation at the interface, being an essential actor in controlling hysteresis and pre-treatment dependence in time transient experiments.

EXPERIMENTAL PROCEDURES

Solar cell fabrication.

Perovskite solar cells were fabricated on F-doped SnO_2 (NSG10) substrates previously cleaned by a sequential sonication treatment in a 2 % Hellmanex solution, acetone and isopropanol, followed by UV ozone treatment for 15 min. These substrates were directly used as described for the ETL-free perovskite solar cells. To prepare the other configurations investigated in this manuscript, a compact blocking layer of TiO_2 (c-TiO_2, 30 nm in thickness) was deposited by spray pyrolysis, using a titanium diisopropoxide bis(acetylacetonate) solution in ethanol (22% v/v), and then sinter at 450 °C for 20 minutes (c-TiO_2 electrode). SnO_2 electrodes were prepared by spin-coating a

precursor solution of $SnCl_4$ (Acros) dissolved in water. To form ~100 nm thick SnO_2 layer, 0.5 M $SnCl_4$ solution was spin-coated on the UV-ozone treated FTO substrates at 5,000 rpm for 10 s. Then the SnO_2 film was transferred onto a hotplate and dried at 100 ^oC for 1 min, post-annealed at 180 ^oC for 1 h and cooled down before deposition of perovskite. The planar configurations, including the ETL-free cells, were treated by UV ozone for 15 min before deposition of perovskite layer. Finally, a 150 nm thick layer of mesoporous TiO_2 (meso-TiO_2, 30 NR-D titania paste from Dyesol) was prepared by spin-coating a diluted TiO_2 dispersion in ethanol (150 $mg \cdot ml^{-1}$), at 2000 rpm for 15 s followed by a sintering step at 450 °C for 30 min. Afterwards, the meso-TiO_2 substrates were lithium-treated by spin-coating 40 µl of tris(bis(trifluoromethylsulfonyl)imide) (Li-TFSI, 10mg/ml in acetonitrile) onto the mesoporous layer, followed by an additional sintering step at 450 °C for 20 min. After sintering, the c-TiO_2/meso-TiO_2 electrodes were ready to use and transferred to a N_2 controlled atmosphere. The perovskite precursor solution was prepared by mixing CH_3NH_3I (MAI, Dyesol) and PbI_2 (TCI) in N,N'-dimethylsulfoxide (DMSO) in a molarity of 1.20 for $MAPbI_3$, while for the mixed cation/halide composition formamidinium iodide (FAI), MAI (from Dyesol), PbI_2 and $PbBr_2$ (TCI) were mixed in DMF:DMSO (4:1) solvent at 1.25 M to form $(FAPbI_3)_{0.85}(MAPbBr_3)_{0.15}$, with 5% of PbI_2 excess content. The perovskite layers were then fabricated by using a two-steps spin-coating process reported by Seok *et al.*[11] (first step 1,000 r.p.m. for 10s; second step 4,000 r.p.m for 30 s) and 10 s prior to the end of the program 100 µl of chlorobenzene were poured onto the films. The substrates were then annealed at 100 °C during 60 min. Afterwards, Spiro-OMeTAD was spin-coated at 4000 rpm from a chlorobenzene solution (28.9mg in 400µl, 60mmol) containing Li-TFSI (7.0µl from a 520 mg/ml stock solution in acetonitrile), TBP (11.5µl) and

Co(II)TFSI (10 mol %, 8.8 µl from a 40 mg/ml stock solution) as dopants. Finally, a 70 nm gold electrode was evaporated.

Thin film characterization

The XRD patterns of the prepared films were measured using a D8 Advance diffractometer from Bruker (Bragg-Brentano geometry, with an X-ray tube Cu Kα, λ=1.5406Å). The absorption spectra were registered with an UV-VIS-IR spectrophotometer (*PerkinElmer Instrument*). Photoelectron spectroscopy (PES) measurements were performed in a ultra-high vacuum analysis chamber (base pressure of 2 x 10^{-10} mbar) using a He-discharge UV source (Omicron) with an excitation energy of 21.2 eV for UPS. Before the analysis, the samples were treated by UV-ozone for 15 in the same conditions as for the device preparation. The photoelectron spectra were recorded using a Phoibos 100 (Specs) hemispherical energy analyzer at a pass energy of 5 eV for the valence band. For work function determination, the secondary electron cut-off (SECO) was recorded by applying a -10 V sample bias to clear the analyzer work function. The reported valence band spectra were background subtracted. The binding energies for all the photoemission spectra are referenced to the Fermi level. For the ns-Transient Absorption Spectroscopy (TAS)/Photoluminescence a ns laser (5ns pulse duration, 10Hz, *Ekspla NT342 model*) with an integrated OPO system (from 355 to 2500 nm tunability) has been used as pump source. It is coupled with the *LP980-KS* Laser Flash Photolysis Spectrometer used for the measurement of laser induced transient absorption, and Photoluminescence kinetics and spectra. Wavelength specific kinetic measurements are made using photomultiplier and digital storage oscilloscope. The probe light is provided by a pulsed Xenon arc lamp. The beams are focused onto the sample on a diameter of minimum 5mm^2 area, ensuring the spatial overlap. The transmitted probe is spectrally filtered by a monochromator and detected. From the

transmission change following photoexcitation the variation in the absorption is thus derived as $\Delta(\tau,\lambda)=\log(I_{probe})/(I_{t(\tau,\lambda)})$, where I_{probe} is the transmitted probe with excitation off and I_t is the transmitted probe after laser excitation. The minimum detectable optical density of the LP980-KS using the photomultiplier is ΔOD = 0.002 (single shot, fast detector option) with a system overall response function of: <7ns (laser limited).

Device characterization

The photovoltaic device performance was analyzed using a VeraSol LED solar simulator (Newport) producing 1 sun AM 1.5 (1000W/m^2) sunlight. Current-voltage curves were measured in air with a potentiostat (Keithley 2604). The light intensity was calibrated with a NREL certified KG5 filtered Si reference diode. The solar cells were masked with a metal aperture of 0.16 cm^2 to define the active area. Current-voltage curves at different scan rates were collected from slowest to fastest scan rate by scanning in the FR direction followed by the RF direction for a given scan rate, with a time interval of 10 seconds (under illumination) before the next measurement. The starting voltage for the FR scan was slightly higher (30 mV) than the V_{oc} of the device while for the RF scan, it was 0 V. EQE was measured with the IQE200B (Oriel) without bias light. Impedance spectroscopy measurements were performed in the dark for a cell area of 0.56 cm^2. A perturbation amplitude of 10 mV was used and the spectra measured over the frequency range 50 mHz – 1 MHz.

ACKNOWLEDGMENTS

SR acknowledges Generalitat Valenciana for the grant GRISOLIA/2014/034. JB acknowledges funding from MINECO of Spain under Project MAT2016-76892-C3-1-R and Generalitat Valenciana Project PROMETEOII/2014/020. MKN acknowledge financial support European Commission H2020-ICT-2014-1, SOLEDLIGHT project,

grant agreement N1: 643791 and the Swiss State Secretariat for Education, Research and Innovation (SERI),and CTI 15864.2 PFNM-NM, Solaronix, Aubonne, Switzerland.

AUTHOR CONTRIBUTIONS

S.G. and C.R. fabricated the devices and carried out the majority of measurements. S.R. performed the impedance analysis. G.G. carried out the spectroscopic analysis. Y.L. prepared the SnO_2 electrodes and mixed cation perovskite layers. M.R and N.K. performed the UPS characterization. C.R., J. B. and M. N. wrote the manuscript and interpreted the data. A. A. assisted in data analysis, and M.N. directed and supervised the project leading to this publication.

DECLARATION OF INTEREST

The authors declare no competing financial interest

REFERENCES

1 Shin, S. S. *et al.* Colloidally prepared La-doped BaSnO3 electrodes for efficient, photostable perovskite solar cells. *Science* **356**, 167-171 (2017).

2 Xiao, Z. *et al.* Efficient perovskite light-emitting diodes featuring nanometre-sized crystallites. *Nat. Photon.* **11**, 108-115 (2017).

3 Fang, Y., Dong, Q., Shao, Y., Yuan, Y. & Huang, J. Highly narrowband perovskite single-crystal photodetectors enabled by surface-charge recombination. *Nat. Photon.* **9**, 679 (2015).

4 Senanayak, S. P. *et al.* Understanding charge transport in lead iodide perovskite thin-film field-effect transistors. *Sci. Adv.* **3**, e1601935 (2017).

5 Xu, J., Chen, Y. & Dai, L. Efficiently photo-charging lithium-ion battery by perovskite solar cell. *Nat. commun.* **6**, 8103 (2015).

6 Xing, G. *et al.* Long-Range Balanced Electron- and Hole-Transport Lengths in Organic-Inorganic CH3NH3PbI3. *Science* **342**, 344-347 (2013).

7 Zhu, H. *et al.* Lead halide perovskite nanowire lasers with low lasing thresholds and high quality factors. *Nat. mater.* **14**, 636 (2015).

8 Kagan, C., Mitzi, D. & Dimitrakopoulos, C. Organic-inorganic hybrid materials as semiconducting channels in thin-film field-effect transistors. *Science* **286**, 945-947 (1999).

9 Ravishankar, S. *et al.* Surface polarization model for the dynamic hysteresis of perovskite solar cells. *J. Phys. Chem. Lett.* **8**, 915-921 (2017).

10 Shen, H. *et al.* Inverted Hysteresis in CH3NH3PbI3 Solar Cells: Role of Stoichiometry and Band Alignment. *J. Phys. Chem. Lett.* (2017).

11 Tress, W. *et al.* Understanding the rate-dependent J-V hysteresis, slow time component, and aging in CH3NH3PbI3 perovskite solar cells: the role of a compensated electric field. *Energy Environ. Sci.* **8**, 995-1004, (2015).

12 Richardson, G. *et al.* Can slow-moving ions explain hysteresis in the current–voltage curves of perovskite solar cells? *Energy Environ. Sci.* **9**, 1476-1485 (2016).

13 Burschka, J. *et al.* Sequential deposition as a route to high-performance perovskite-sensitized solar cells. *Nature* **499**, 316-319 (2013).

14 Malinkiewicz, O. *et al.* Perovskite solar cells employing organic charge-transport layers. *Nat. Photon.* **8**, 128-132 (2014).

15 Jeon, N. J. *et al.* Compositional engineering of perovskite materials for high-performance solar cells. *Nature* **517**, 476-480 (2015).

16 Park, N.-G. Methodologies for high efficiency perovskite solar cells. *Nano converg.* **3**, 1-13 (2016).

17 Lim, K. G. *et al.* Boosting the Power Conversion Efficiency of Perovskite Solar Cells Using Self-Organized Polymeric Hole Extraction Layers with High Work Function. *Adv. Mater.* **26**, 6461-6466 (2014).

18 Lim, K. G. *et al.* Self-Doped Conducting Polymer as a Hole-Extraction Layer in Organic–Inorganic Hybrid Perovskite Solar Cells. *Adv. Mater. Interfaces* **3,** (2016).

19 Lim, K.-G., Ahn, S., Kim, Y.-H., Qi, Y. & Lee, T.-W. Universal energy level tailoring of self-organized hole extraction layers in organic solar cells and organic–inorganic hybrid perovskite solar cells. *Energy Environ. Sci.* **9**, 932-939 (2016).

20 Gottesman, R. *et al.* Dynamic Phenomena at Perovskite/Electron-Selective Contact Interface as Interpreted from Photovoltage Decays. *Chem* **1**, 776-789 (2016).

21 Rong, Y. *et al.* Solvent engineering towards controlled grain growth in perovskite planar heterojunction solar cells. *Nanoscale* **7**, 10595-10599 (2015).

22 Juarez-Perez, E. J. *et al.* Role of the selective contacts in the performance of lead halide perovskite solar cells. *J. Phys. Chem. Lett.* **5**, 680-685 (2014).

23 Kim, H.-S. & Park, N.-G. Parameters Affecting I–V Hysteresis of CH3NH3PbI3 Perovskite Solar Cells: Effects of Perovskite Crystal Size and Mesoporous TiO2 Layer. *J. Phys. Chem. Lett.* **5**, 2927-2934 (2014).

24 Sanchez, R. S. *et al.* Slow dynamic processes in lead halide perovskite solar cells. Characteristic times and hysteresis. *J. Phys. Chem. Lett.* **5**, 2357-2363 (2014).

25 Garcia-Belmonte, G. & Bisquert, J. Distinction between capacitive and noncapacitive hysteretic currents in operation and degradation of perovskite solar cells. *ACS Energy Lett.* **1**, 683-688 (2016).

26 Zarazua, I., Bisquert, J. & Garcia-Belmonte, G. Light-induced space-charge accumulation zone as photovoltaic mechanism in perovskite solar cells. *J. Phys. Chem. Lett.* **7**, 525-528 (2016).

27 Ghahremanirad, E., Bou, A., Olyaee, S. & Bisquert, J. Inductive Loop in the Impedance Response of Perovskite Solar Cells Explained by Surface Polarization Model. *J. Phys. Chem. Lett.* **8**, 1402-1406 (2017).

28 Berera, R., van Grondelle, R. & Kennis, J. T. Ultrafast transient absorption spectroscopy: principles and application to photosynthetic systems. *Photosynth. Res.* **101**, 105-118 (2009).

29 Leijtens, T. *et al.* Carrier trapping and recombination: the role of defect physics in enhancing the open circuit voltage of metal halide perovskite solar cells. *Energy Environ. Sci.* **9**, 3472-3481 (2016).

30 Li, W., Liu, J., Bai, F.-Q., Zhang, H.-X. & Prezhdo, O. V. Hole Trapping by Iodine Interstitial Defects Decreases Free Carrier Losses in Perovskite Solar Cells: A Time-Domain Ab Initio Study. *ACS Energy Lett.* **2**, 1270-1278 (2017).

Figure Captions

Figure 1. **Solar cell configurations, film characterization and photovoltaic performance of the perovskite cells. (A)** Schematic diagram of the cell architectures. Compact and mesoposous-TiO_2 (meso-TiO_2) layers are differing between configurations. (**B)** cross-sectional scanning electron microscopy (SEM) images

obtained for each representative layout (bar-scale 1µm). (**C)** Surface SEM images and optical properties of perovskite films analysed in (b). (**D)** X-ray diffraction (XRD) patterns of films analysed in (D).

Figure 2. *J-V* performance and statistical analysis of perovskite solar cells. (A) Current-voltage (*J−V*) curves measured under 1 sun illumination and **(B)** external quantum efficiency (*EQE)* of representative solar cells containing meso-TiO_2, c-TiO_2 and *ETL-free* architectures ($J_{integrated}$ is 21.2 mA·cm^2, 21.5 mA·cm^{2}and 21.3 mA·cm^2 for). **(C)** Summary of device parameters obtained for more than 40 cells measured under AM1.5G sun illumination, room temperature and air conditions. The work function of the different contact layers are also indicated for comparison *(right panel).*

Figure 3. Hysteresis behavior and impedance spectroscopy (IS) analysis. **(A)** *J-V* scans for perovskite cells containing the three investigated ETL contacts (scan rates indicated in the legend); **(B)** absolute real values of the capacitance obtained from EIS measurements in the dark; **(C)** evolution of the low frequency capacitance versus applied voltage for the three investigated cells. The linear fit of ln C versus voltage for the ETL-free cell shows a slope of 5.62.

Figure 4. **Dynamical optical investigation using transient absorption spectroscopy (TAS). (A-C)** TAS spectral evolution of the three different samples measured upon excitation from the glass side with an incident light pulse at 600nm (penetration depth ~200 nm)[25]. **(D)** dynamics at 760nm revealing a faster time constant of t=100 ns.

TABLES AND TABLE CAPTIONS

Table 1. **Device parameters obtained from the cell configurations shown in Figure 2.** The average values obtained for each device configuration are included in brackets.

Cell	J_{sc} **(mA · cm^2)**	V_{oc} **(V)**	***FF***	***PCE* (%)**
Meso-TiO_2	21.91 (21.9 ± 0.8)	1.09 (1.078 ± 0.007)	0.78 (0.77 ± 0.02)	18.75 (18.17 ± 0.8)
c-TiO2	21.7 (21.2 ± 0.9)	1.07 (1.02 ± 0.03)	0.70 (0.67 ± 0.05)	16.25 (15 ± 1)
FTO	21.08 (21.1 ± 0.6)	1.04 (0.98 ± 0.08)	0.64 (0.62 ± 0.03)	14.03 (14 ± 1)

Table 2. Optical parameters obtained from the TAS analysis.

Sample	**t1 (ns)**	**t2 (ns)**
FTO/MAPbI3	21	98
FTO/c-TiO2/MAPbI3	13	98
FTO/c-TiO2/MesoTiO2/MAPbI3	50	269

Figures

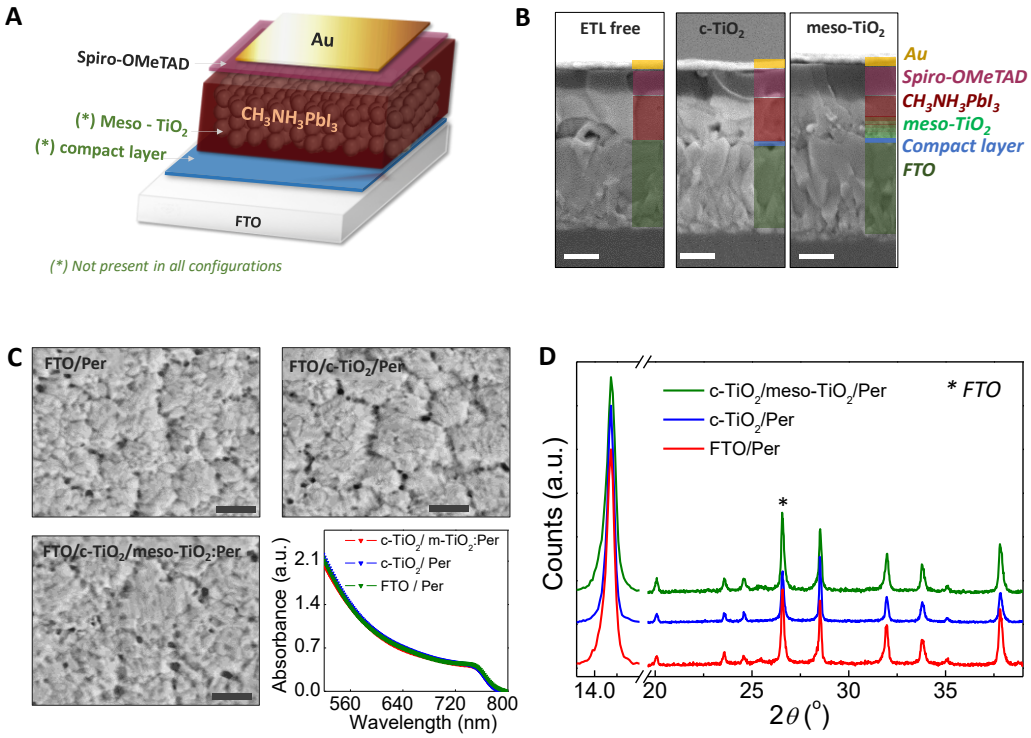

Figure 1.

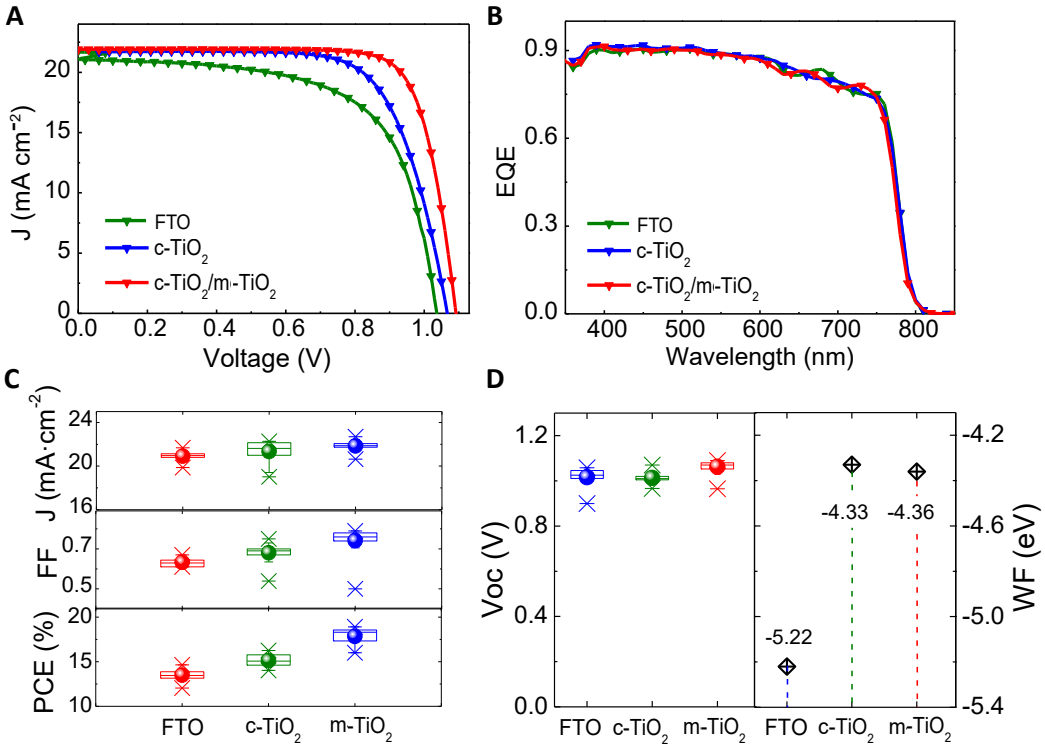
A
J (mA cm-2)
Voltage (V)
FTO
c-TiO2
c-TiO2/m-TiO2
B
EQE
Wavelength (nm)
C
J (mA·cm-2)
FF
PCE (%)
FTO
c-TiO2
m-TiO2
D
Voc (V)
WF (eV)
-5.22
-4.33
-4.36

Figure 2.

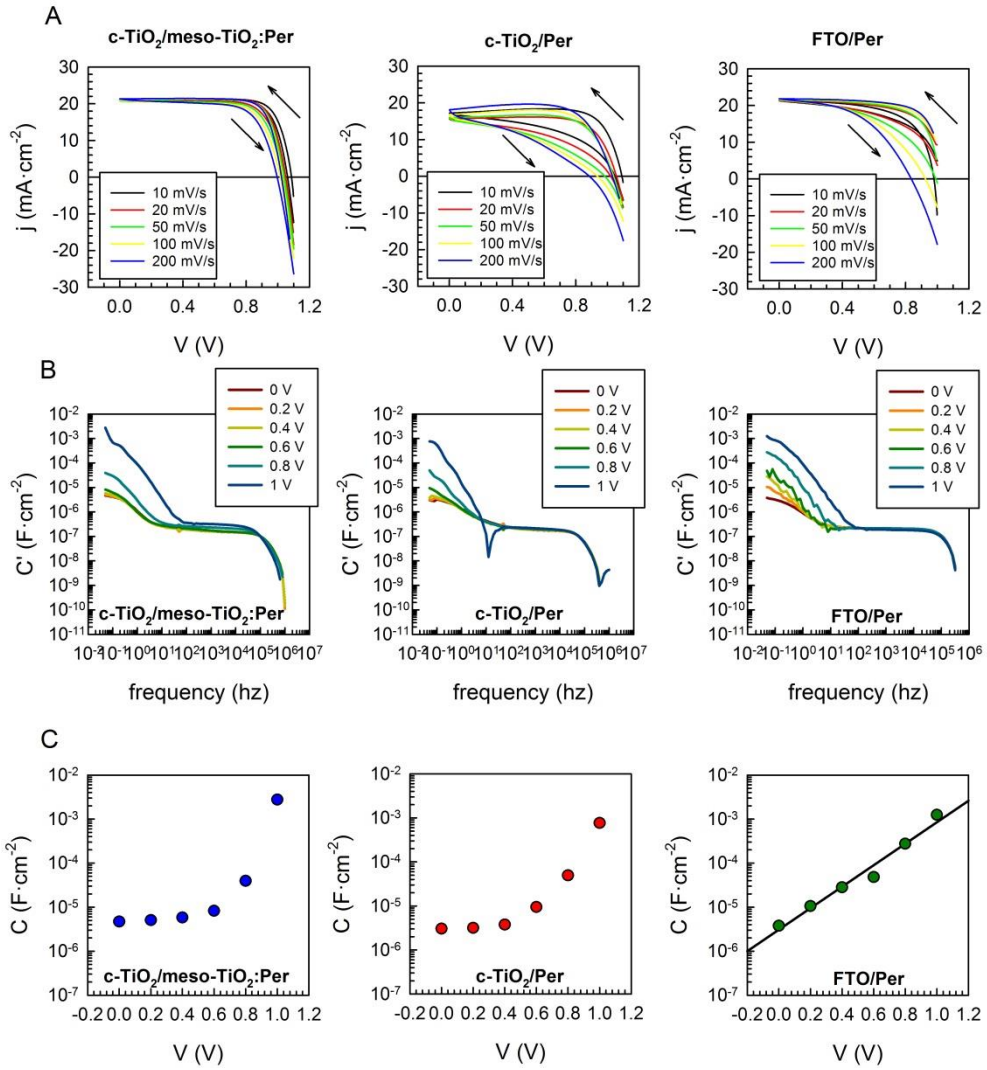
A
c-TiO2/meso-TiO2:Per
c-TiO2/Per
FTO/Per
j (mA·cm-2)
V (V)
10 mV/s
20 mV/s
50 mV/s
100 mV/s
200 mV/s
B
C' (F·cm-2)
frequency (hz)
0 V
0.2 V
0.4 V
0.6 V
0.8 V
1 V
C
C (F·cm-2)

Figure 3.

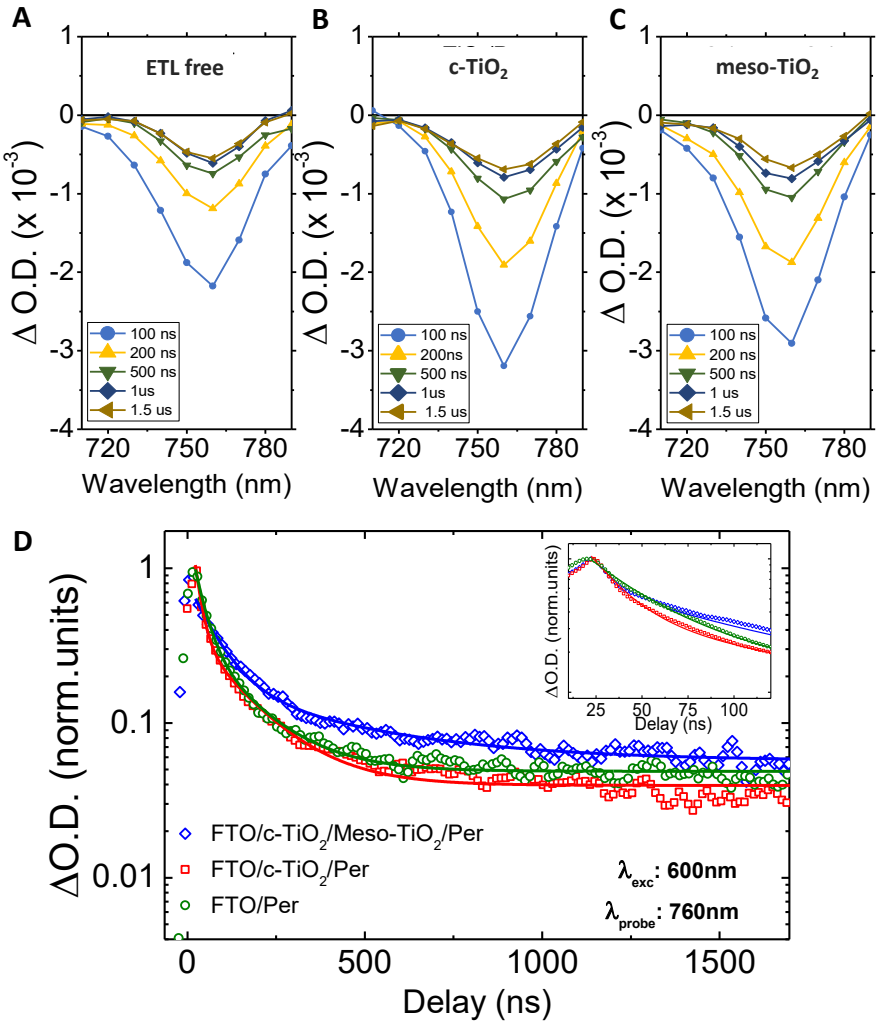
A
ETL free
B
c-TiO2
C
meso-TiO2
Δ O.D. (x 10-3)
Wavelength (nm)
100 ns
200 ns
500 ns
1us
1.5 us
D
ΔO.D. (norm.units)
Delay (ns)
FTO/c-TiO2/Meso-TiO2/Per
FTO/c-TiO2/Per
FTO/Per
λexc: 600nm
λprobe: 760nm

Figure 4.